

Heteroepitaxy with PbSe nanocrystals enables highly stable wide-bandgap perovskite solar cells

Yuhui Jiang^{1,5}, Pengfei Guo^{1,5}, Ruihao Chen¹, Liming Du¹, Xingchao Shao², Xiuhai Zhang¹, Yu Zheng¹, Ning Jia¹, Zhiyu Fang¹, Luyao Ma¹, Xu Zhang¹, Zhen Li¹, Yi Hou³, Fen Lin³, Chunlei Yang², Weimin Li^{2,*}, Zhe Liu^{1,4,*}, Hongqiang Wang^{1,*}

¹School of Materials Science and Engineering, Northwestern Polytechnical University, 127 Youyi West Road, Xi'an, Shaanxi, P.R. China 710072

²Shenzhen Institute of Advanced Technology, Chinese Academy of Sciences, 1068 Xueyuan Avenue, Shenzhen, Guangdong, P.R. China 518055

³Solar Energy Research Institute of Singapore, National University of Singapore, 7 Engineering Drive 1, Singapore, 117574

⁴Clean Energy Institute, NPU Yangtze River Delta Institute, Taicang, Jiangsu, 215400

⁵These authors contributed equally.

*Corresponding authors: wm.li1@siat.ac.cn; zhe.liu@nwpu.edu.cn; hongqiang.wang@nwpu.edu.cn

Hybrid halide perovskite materials with tunable bandgaps have long been regarded as prime candidates for tandem solar cells. However, the increase in bromine (Br) content often leads to photoinduced halide phase segregation, reducing the overall performance of tandem solar cells. Here we prepare PbSe nanocrystals (NCs) using liquid-phase pulsed laser (LPPL) processing and incorporate them into wide-bandgap perovskite to interact with Pb-halide octahedra. Through the interaction in the precursor solution, the competitive nucleation of halides is regulated, leading to the formation of perovskite. The heteroepitaxial perovskite film due to its excellent uniformity and defect-free characteristics, exhibits no halide phase segregation under illumination as the tightly connected perovskite lattice lacks ion migration paths. Furthermore, we achieved a remarkable power conversion efficiency (PCE) of 22.87 % for wide-bandgap (1.68 eV) perovskite ($\text{Cs}_{0.05}(\text{FA}_{0.77}\text{MA}_{0.23})_{0.95}\text{Pb}(\text{I}_{0.77}\text{Br}_{0.23})_3$) *p-i-n* devices. The unencapsulated cells maintain 79 % of their initial efficiency after 1000 hours of light soaking under an open circuit. Additionally, by stacking the semi-transparent perovskite cells and CIGS, the tandem cell achieved a PCE of 28.24 %.

Introduction

The perovskite-based dual-junction solar cells, such as perovskite/silicon or perovskite/CIGS tandems, have garnered significant attention to increase solar energy utilization and surpass the PCE limit of single-junction cells^{1, 2, 3}. To maximize the overall efficiency of tandem cells, it is important to make the bandgap of perovskite top cell to fall within the range of 1.65 to 1.7 eV. Therefore, mixed-halide perovskite top

cells are commonly employed, and the bandgap can be easily tuned by introducing bromide into the iodide-based perovskite lattice^{4, 5, 6, 7}. However, the increased Br content induces lattice contraction due to the decrease in the average bond distance of Pb-X⁸. Under illumination, the deformed lattice results in the generation of more electron-hole pairs, which accelerate the rearrangement of halogen anions (*i.e.*, Br and I), resulting in the formation of spatially separated Br-rich and I-rich domains, which is known as phase segregation^{9, 10}. The photoinduced phase segregation in the wide-bandgap perovskite can easily cause a significant loss in the open-circuit voltage, which thereafter degrades the photovoltaic (PV) device PCE over a short period^{11, 12}. Therefore, tackling the photoinduced phase segregation in wide-bandgap perovskite solar cells is an essential prerequisite for the potential commercialization of perovskite-based tandem solar cells.

A deep understanding of the mixed halide perovskite formation process, from precursor to film, can provide insights for preventing phase segregation. In the perovskite precursor, Pb-Br bonds exhibit greater strength compared to Pb-I bonds¹³, leading to preferential nucleation and growth of Br-containing intermediate phases. As illustrated in **Fig. 1a**, competitive nucleation leads to uneven initial crystallization, resulting in a plethora of halogen vacancy defects. Under photo-illumination, the unevenness in initial crystallization results in the strain gradient^{14, 15, 16}, attracting I with a tendency to migrate and forming I-rich phases, which finally leads to phase segregation.

Thus far, it has been widely recognized that the initial inhomogeneity^{17, 18, 19, 20, 21} and the presence of halide vacancy^{22, 23} play pivotal roles in the phase segregation of perovskite thin films. On one hand, for instance, Bai *et al.* recently revealed that initial film inhomogeneity leads to rapid degradation, where the formation of the two phases follows the general guidance of Schelling's model²⁴. By adding selenophene in the precursor to regulate the crystallization process, the homogeneity of perovskite film was significantly improved, therefore enhancing the stability of perovskite PV devices with varied compositions. On the other hand, defect passivation strategies aim to “cut off” the pathways of halide migration by reducing halide vacancies^{25, 26, 27}. These vacancy reduction strategies primarily involve surface and bulk defect passivation with organic molecules^{28, 29} or salts^{30, 31}. For example, Yang *et al.* identified positive iodide interstitials as the important defects and added tribromide to occupy the halide site reducing the defects concentration²⁹. Wang *et al.* added adenosine triphosphate to suppress ion migration by relaxing residual strain³². Thus, the ideal way to address the phase segregation challenge is to achieve a homogeneous crystallization process for halide-vacancy-free perovskite thin films.

Inspired by the concept of “quantum-dots-in-perovskite solids” concept proposed by Ning & Sargent *et al.*³³, we believe it is possible to achieve better control of perovskite crystallization via heteroepitaxial growth mechanism when PbX-based (X=S, Se, Te, etc.) nanocrystals (NCs) is present in the mixed-halide perovskite precursor. We hypothesize that the perovskite growth could be regulated by the NCs as nucleation seeds. When adding the NCs into the precursor, the NCs attract

uncoordinated Pb ions due to their functionalized surface state, which in turn induces the formation of Pb-X bonds and attracts the intermediate phase of Pb-halide octahedra. This binding orientation causes the Pb-halide intermediates to surround the NCs, leading to the formation of perovskite. The heteroepitaxial growth processing controls the crystallization, resulting in high-quality perovskite film with anchored wide-bandgap perovskite lattice and reduced vacancy defects. Under illumination, the migration barrier of halogens increases, suppressing phase segregation (**Fig. 1b**). To realize this idea, we leverage a unique laser fabrication capability for meta-stable PbX NCs in a liquid solution, called liquid-phase pulsed laser (LPPL) processing (**Fig. S1 in Supplementary Information**). Our previous works have demonstrated the success of the LPPL process as an easy method to fabricate different types of NCs^{34, 35, 36, 37}, and add them into perovskite thin films via precursors or antisolvents. In recent work, we also investigated the fabrication of PbX NCs using LPPL processing and demonstrated the possibility of incorporating the NCs into perovskite lattice.

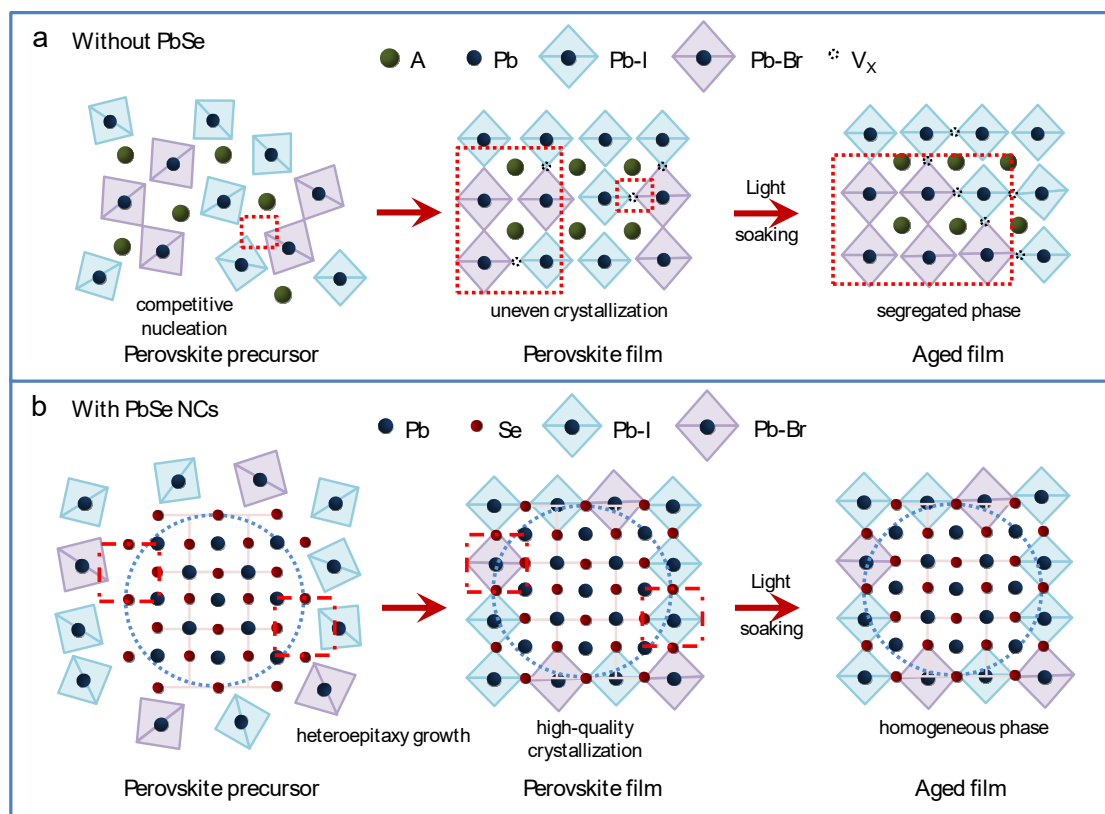


Fig. 1 Schematic illustration of crystallization process and stability under illumination. a. The typical mixed-halide perovskite with inhomogeneous crystallization with formation of vacancy defects. **b.** The mechanism of the heteroepitaxial-grown mixed-halide perovskite with the incorporation of the PbX NCs.

In this study, we utilize PbSe NCs to control the crystallization of the mixed-halide perovskite and achieve highly efficient and stable mixed-halide wide-bandgap perovskite devices. Particularly, we focus on exploring the possibility of heteroepitaxial crystallization control with PbSe NCs to suppress photoinduced phase segregation in mixed-halide perovskite. In perovskite precursor solution, the PbSe NCs attract Pb-

halide octahedra, causing them to grow along the NCs and bind with Pb multiple bonds, thereby reaching high-quality crystallization with more uniform films. Under illumination, the activation energy barrier of ion migration increases, and no phase segregation in PbSe-embedded film is observed over five days. At the same time, the device performance and light stability have been significantly improved.

Results and discussion

Properties of PbSe nanocrystals and incorporation into perovskite films

The PbX NCs were synthesized by LPPL and incorporated into mixed-halide perovskite. There are no crystallographic plane changes in the perovskite films with PbX NCs (**Fig. S2**). The films were exposed to 1-sun continuous light soaking (LED lamp, 45 °C) for 15 h. The PbSe-embedded film has demonstrated superior photostability³⁸, as evidenced by the X-ray diffraction instrument (XRD), as shown in **Fig. S3**. Based on these initial screening results of photostability, we focus on the PbSe NCs as an example of in-depth analysis.

To incorporate the PbSe NCs into the wide-bandgap perovskite lattice, it is imperative to first synthesize the NCs with precisely controlled particle sizes in the desired solvent^{35, 39} (e.g., DMF and DMSO mixed solvent in our study). Stable and well-dispersed PbSe NCs with an average diameter of 3 nm were successfully obtained, as depicted in **Fig. 2a** via the high-angle angular dark-field transmission electron microscopy (HAADF-TEM). Further structural analysis of the PbSe NCs was conducted using high-resolution transmission electron microscopy^{36, 40} (HRTEM). The lattice fringes, with a spacing of 3.07 Å as illustrated in **Fig. 2b**, were affiliated the characteristic plane (200) of PbSe.

Mapping determined by TEM-energy dispersive spectroscopy (TEM-EDS) revealed the absence of oxygen (O) elements during the laser process. Additionally, in comparison to Pb elements, Se was found to be more abundant within the PbSe NCs (**Fig. 2c**), demonstrating the Se-rich characteristics⁴¹. To further characterize this feature, X-ray photoelectron spectroscopy (XPS) was employed to investigate the NCs. As profiled in **Fig. S4**, the level peaks of Se 3d shifted to higher binding energy^{42, 43} in PbSe NCs, as compared with PbSe powders, indicating the presence of Se²⁻ within NCs. Conversely, the negligible shift was observed for the peaks⁴⁴ of PbSe 3d_{5/2} and 3d_{3/2}. By analyzing the area of different compositions in the XPS spectrum, we found that Se²⁻ constitutes 29 % in the PbSe NCs (**Fig. S5**), further confirming the Se-rich characteristics. Similarly, the XRD patterns also revealed the Se-rich feature, as shown in **Fig. S6**. Comparing the main diffraction peak of PbSe powders^{44, 45} at 29.14°, the peak of PbSe NCs shifts, attributed to the diffraction peaks of Se at 29.45°.

To investigate the stability of the NCs colloidal solution, we introduced zeta potential, as it serves as a measure of the strength of the mutual repulsion or attraction between particles⁴⁶. The more negative zeta potential value of the PbSe NCs colloidal solution compared to the pristine PbSe system, shifting from -16 mV to -31 mV, indicated greater repulsive forces between colloidal particles (**Fig. S7**). The negative

zeta potential of the solution indicates the presence of negative charges on the surface of the PbSe NCs. The smaller the PbSe NCs, the higher the absolute value of the zeta potential, leading to a more stable system⁴⁷. All the analyses above demonstrate that PbSe NCs with controllable size can be prepared using LPPL.

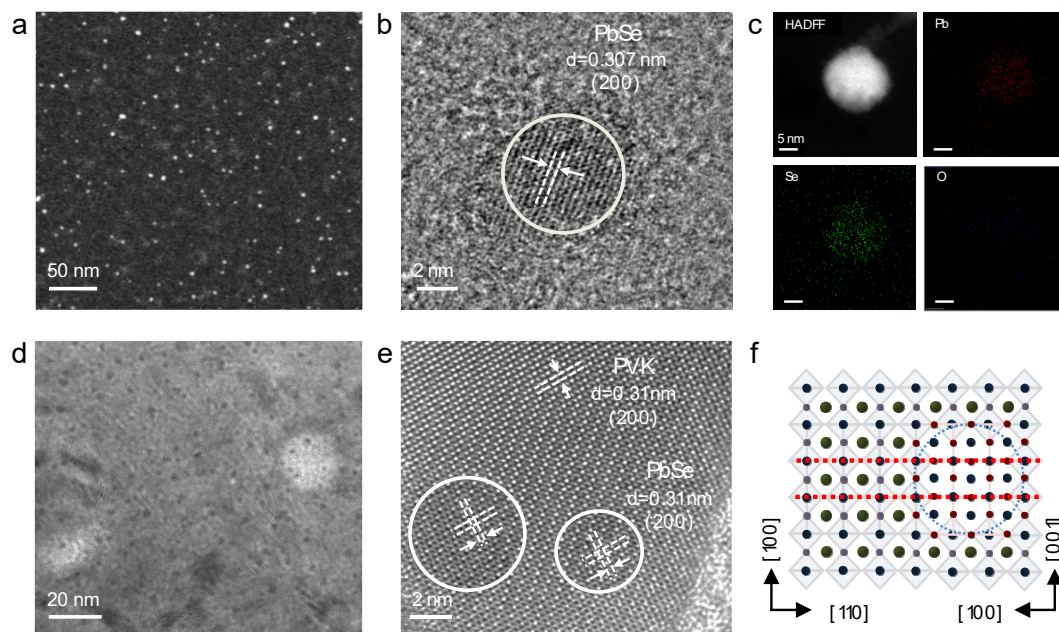


Fig. 2 The properties of the PbSe nanocrystals and the PbSe-embedded film. **a.** The HAADF image of the PbSe NCs (white spots). **b.** The HRTEM image and **c.** Corresponding TEM-EDS of the PbSe NCs. **d.** The cross-sectional TEM image of the PbSe-embedded film and **e.** the corresponding HRTEM images. **f.** The structure of the PbSe NCs embedded film. The red dashes show that the perovskite unit cell size matches well with PbSe.

To confirm the possibility of heteroepitaxial growth, we utilized TEM to study the perovskite films and their cross-sections. As shown in the **Fig. S8** and **Fig. 2d**, compared to the control film, the PbSe NCs were uniformly distributed within the perovskite, and their size was consistent with that in the solution, measuring 3-5 nm. Further, the HRTEM was employed to determine the positioning of PbSe within the perovskite films (**Fig. 2e**). In the selected area, the lattice spacings of the PbSe (200) planes and the perovskite (200) planes were found to be identical, with PbSe being embedded within the perovskite film (**Fig. 2f**). The same lattice spacing further substantiates the heteroepitaxial growth of perovskite along the PbSe nanocrystals.

Subsequently, we optimized the PbSe NCs concentrations to enhance the film and the device performance. Firstly, as the small white spots on the surface can be observed at the higher concentration (0.03 and 0.04 mg/mL) in the scanning electron microscope (SEM) images (**Fig. S9**), we set the concentration range to be 0.01 to 0.03 mg/mL. Furthermore, atomic force microscope (AFM) was used to exhibit the lowest RMS roughness of the 0.015 mg/mL, compared to the control, with a reduction from 15.87 to

11.94 nm, as depicted in **Fig. S10**. Finally, we proceed to investigate the effect of different concentrations on the photovoltaic performance in the devices, employing a planar *p-i-n* device structure consisting of glass/ ITO/ NiO_x/ MeO-2PACz /perovskite /C60 /BCP /Ag. The decrease in fill factor at the higher concentrations (0.03 mg/mL) may be related to the defects of the enriched white spots surface (**Fig. S11**). The statistical distribution of the control device and the devices with different concentrations from the 15 cells in the same batch are summarized in **Fig. S12** and **Table S1**. It was found that the film at 0.015 mg/mL exhibited the best performance.

Suppression of phase segregation with PbSe nanocrystals

To visualize the impact of controlling crystallization by the PbSe NCs on the evolution of the perovskite phase segregation under illumination, photoluminescence (PL) spectroscopy was used in conjunction with XRD and SEM.

As depicted in **Fig. 3a** and **Fig. 3d**, the PL characteristic emission of the control and PbSe films were at 736 nm. After one day of 1-sun light soaking, the control film exhibited broadening with a peak at 741 nm. Over subsequent days of light soaking, the film further experienced a redshift, ultimately reaching a peak at 768 nm by the fifth day. In contrast, there was no noticeable shift in the fluorescence peak of the PbSe film, with only a slight change observed from 736 to 738 nm (the 0.015mg/ml in **Fig. S13**). The significant peak redshift in the control film was mainly ascribed to the formation of I-rich domains^{23, 48, 49, 50} under light soaking.

XRD analysis suggests that the addition of PbSe NCs suppresses the formation of lead (II) iodide (PbI₂), and the transition from tensile to compressive strain^{51, 52} can be found using the Williamson-Hall method (**Fig. S14**). The parameters obtained from the films were given in **Table S2** and **Table S3**. Finally, we accurately analyzed the XRD diffraction peaks of the perovskite crystallographic planes of (200) and (211) before and after 30 hours of light soaking. Upon illumination, the XRD peak of the control film split (**Fig 3b**), indicating the characteristic peak of the I-rich and Br-rich phase³⁸. However, there was no significant change in the PbSe film, for the absence of phase segregation.

The SEM images of both the control and PbSe-embedded films are shown in **Fig. 3c** and **Fig. 3f**, the embedment of PbSe NCs regulated the in-situ formation of Pb-halide octahedra during the nucleation process of perovskite, resulting in smoother perovskite films and larger grain sizes. After 30-hour light soaking utilizing a LED lamp (1-sun), the surface of the control film exhibited corrosion, with increased white flakes at the grain boundaries, showing the characteristics of iodine phase enrichment⁵³. However, this phenomenon was not evident in the PbSe film. It paralleled visual degradation (**Fig. S15**), manifesting as black spots on the surface of the control film, while there was no significant change in the PbSe film. The morphological changes before and after light soaking provided preliminary evidence that PbSe NCs effectively inhibit phase segregation. These results suggest that the defect passivation by PbSe NCs effectively suppresses phase segregation and provides superior photostability.

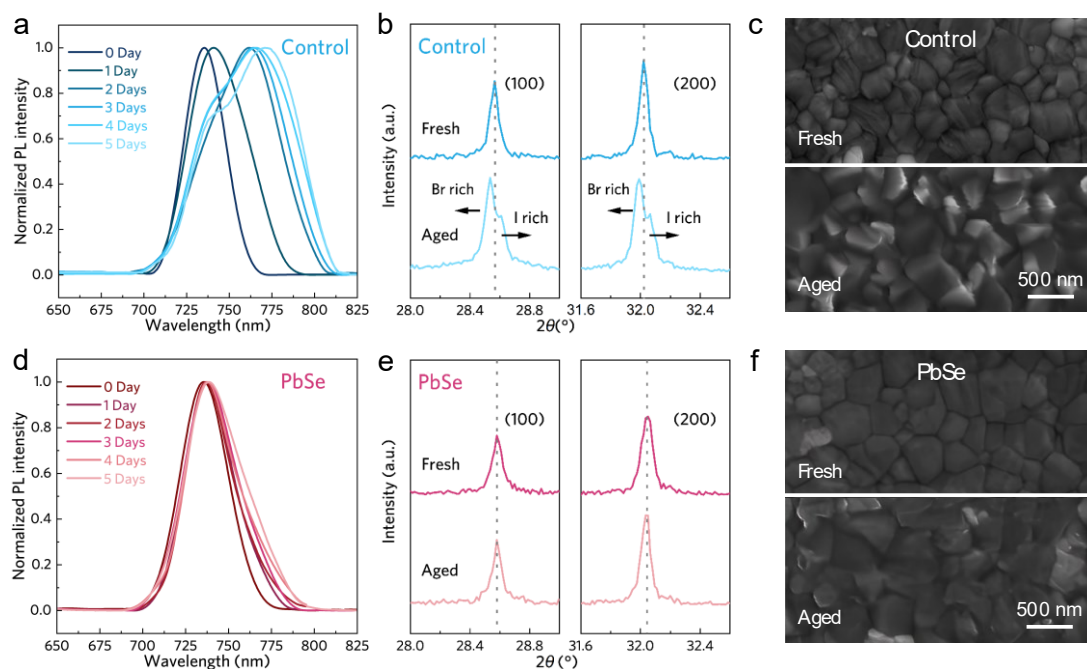


Fig. 3 Characterization of phase segregation. Photo-induced phase segregation investigation of **a.** the control and **d.** the PbSe-embedded film by PL measurements. The XRD images of **b.** the control and **e.** the PbSe-embedded film (30 h light soaking). The fresh and the aged (30 h light soaking) SEM images of **d.** the control and **f.** the PbSe-embedded film. The illumination light source is a LED lamp with an intensity of 1-sun. The sample temperature is approximately 45 °C.

The Presence of PbSe in Mixed-Halide Perovskite Thin Films

To elucidate the impact of PbSe embedment on the perovskite film, we initially employed ultraviolet-visible (UV-vis) spectroscopy. The images in **Fig. S16** demonstrated enhanced light absorption⁵⁴ of the PbSe-embedded film. Additionally, no significant changes were observed at the absorption edges of both films, indicating that the perovskite bandgap⁵⁵ remained at 1.68 eV. Both PL and confocal microscopy images (**Fig. S17**) revealed a significant emission enhancement in the PbSe-embedded film^{56, 57}. We also utilized X-ray photoelectron spectroscopy (XPS) and ultraviolet photoelectron spectroscopy (UPS) to analyze the chemical environment of components within perovskite^{34, 48} and the influence of PbSe on the energy level. As shown in **Fig. 4a** and **Fig. 4b**, the core level peaks of Pb 4f and I 3d exhibited shifts to lower binding energies in PbSe films compared to control films, indicating a direct interaction between PbSe NCs and Pb²⁺ ions by occupying halide vacancies⁵⁸. The UPS images as shown in **Fig. 4c** reveal a shift in the Fermi level (E_F) from -4.95 eV to -4.85 eV with PbSe embedment, potentially indicating the improved energy levels and regulated, the carrier dynamics, as depicted in Fig. 4d. The primary enhancement of V_{OC} in the wide-bandgap cells stems from the changed Fermi level and the enhanced carrier extraction capability of the transport layer^{32, 59}.

To further ascertain the effect of controlling crystallization on defect passivation, electron-only devices were fabricated to explore the trap-state density through the

space-charge-limited current (SCLC) method^{36, 60} as illustrated in **Fig. 4e**. The calculated trap-state densities of the control and PbSe films are 1.87×10^{16} and $1.37 \times 10^{16} \text{ cm}^{-3}$, respectively. The decrease in defect density corresponds to alterations in the carrier lifetime of the perovskite, highlighting the crucial role of high-quality crystallization with a lower density of defects. An evident prolongation of the average carrier lifetime was achieved in the PbSe NCs perovskite film (**Fig. S18**), and the τ_{ave} increased from 69.67 ns to 128.34 ns, with further details provided in **Table S4**.

To discuss the internal ion migration within the perovskite, the dark-state current density voltage (J - V) characteristics of the perovskite film were investigated by scanning and re-scanning from negative bias (-1 V) to positive bias (1 V)^{35, 61}. Notably, the conductivity has increased by almost four orders of magnitude in **Fig. 4f**, this proved that the charge transfer between grains was promoted, and the carrier mobility improved. Meanwhile, the alignment of the PbSe-embedded J - V curves provided compelling evidence that the NCs embedment facilitates the anchoring of perovskite halide anions, thereby inhibiting phase segregation.

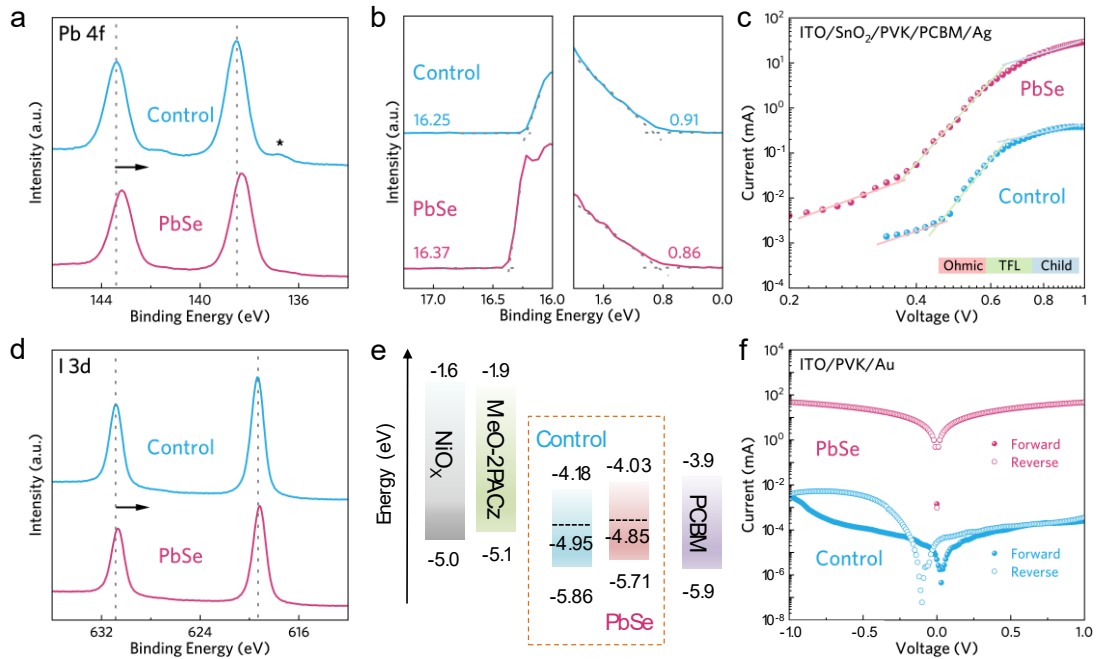


Fig. 4 The properties of the perovskite films. ab. XPS spectra of Pb 4f and I 3d signal for the control and the PbSe-embedded film. **c.** UPS spectra. **d.** Energy level scheme of the control and the PbSe-embedded film. **e.** Dark J - V curves of SCLC measurements. **f.** Logarithmic J - V plots under dark.

Efficient and stable perovskite solar cell

Following, planar p - i - n perovskite solar cells were fabricated to investigate the influence of PbSe embedment on their photovoltaic performance, the structure schematic as shown in **Fig. S19**. The PbSe-embedded devices demonstrated the highest V_{OC} and PCE, as depicted in **Fig. 5a**. The devices employing the p - i - n structure

achieved a champion PCE of 22.87 % with a V_{OC} of 1.25 V, surpassing the performance of control devices which afforded a PCE of 19.45 %. The PbSe-embedded devices also exhibited reduced hysteresis behavior, attributable to high-quality crystallization. The J - V characteristic parameters of 30 perovskite devices were statistically analyzed to confirm the reproducibility of the device performance, as shown in **Fig. 5b**, and the detailed photovoltaic parameters were summarized in **Fig. S20** and **Table S5**. To verify the reliability of J_{SC} , the external quantum efficiency (EQE) measurement was conducted. The integrated current density of the control and PbSe devices were determined to be 20.73 and 21.06 mA/cm² (**Fig. S21**). The improvement in J_{SC} was attributed to more efficient light absorption (**Fig. S16**) and elevated EQE values over the wavelength in comparison to the control film and device^{54, 55}. This collective evidence underscores the effectiveness of PbSe embedment in enhancing the PCEs of perovskite solar cells. It's noteworthy that in the 1.68 eV wide-bandgap perovskite cells, the achieved PCE is close to the thermodynamic potential limit of 80%, as illustrated in **Fig. 5c**.

To assess non-radiative recombination stemming from deep-level defects, the light-intensity-dependent V_{OC} measurement serves as an effective method. The slope of the plot in **Fig. S22** demonstrates a correlation with the ideality factor⁶² (n), with a value of 1.46 observed for the PbSe device, compared to 1.78 for the control device. The decrease in the n value indicated the suppression of defect-assisted non-radiative recombination⁵⁵. As depicted in **Fig. S23**, the transport resistance (R_{CT}) of the PbSe-embedded device decreased compared with the control, indicating an improvement in the carrier transport⁶². Moreover, the dark state J - V curve of perovskite devices before and after embedment, shown in **Fig. S24**, demonstrates a reduced reverse saturation current in the PbSe device, suggesting a reduction in trap states^{36, 60}. The findings indicate promising advancements in mitigating non-radiative recombination and improving carrier transport through PbSe embedment.

Further assessments for the long-term stability of control and PbSe-embedded devices confirm the impact of high-quality crystallization. The maximum power point (MPP) tracking was measured to be 22.24 % under 1-sun illumination, providing further validation of the stability of the PbSe-embedded device under short-term operation (600 s), as illustrated in **Fig. S25**. The thermal stability (85 °C) was shown in **Fig. 5d**, the normalized PCE of the PbSe-embedded device remained above 80 % after 2000 h in a nitrogen atmosphere, whereas the control device dropped below 75 % after only 100 h. In **Fig. 5e**, J - V scans were performed every 30 h under 1-sun light soaking, including both forward and reverse scans, with voltage ranging from -0.1 to 1.3 V. The PbSe-embedded device maintained 79 % PCE after 1000 hours, while the control device quickly degraded to 65 % after 210 hours. The improved photostability originated from the suppressed photo-induced phase segregation in the wide-bandgap perovskite. As shown in **Fig. 5f**, the storage lifetimes of the unencapsulated PbSe devices remained 93 % in the dark under a nitrogen atmosphere after 3000 h, but the control device fell below 90 % after 500 hours. These results underscore the enhanced stability in all aspects conferred by PbSe embedment.

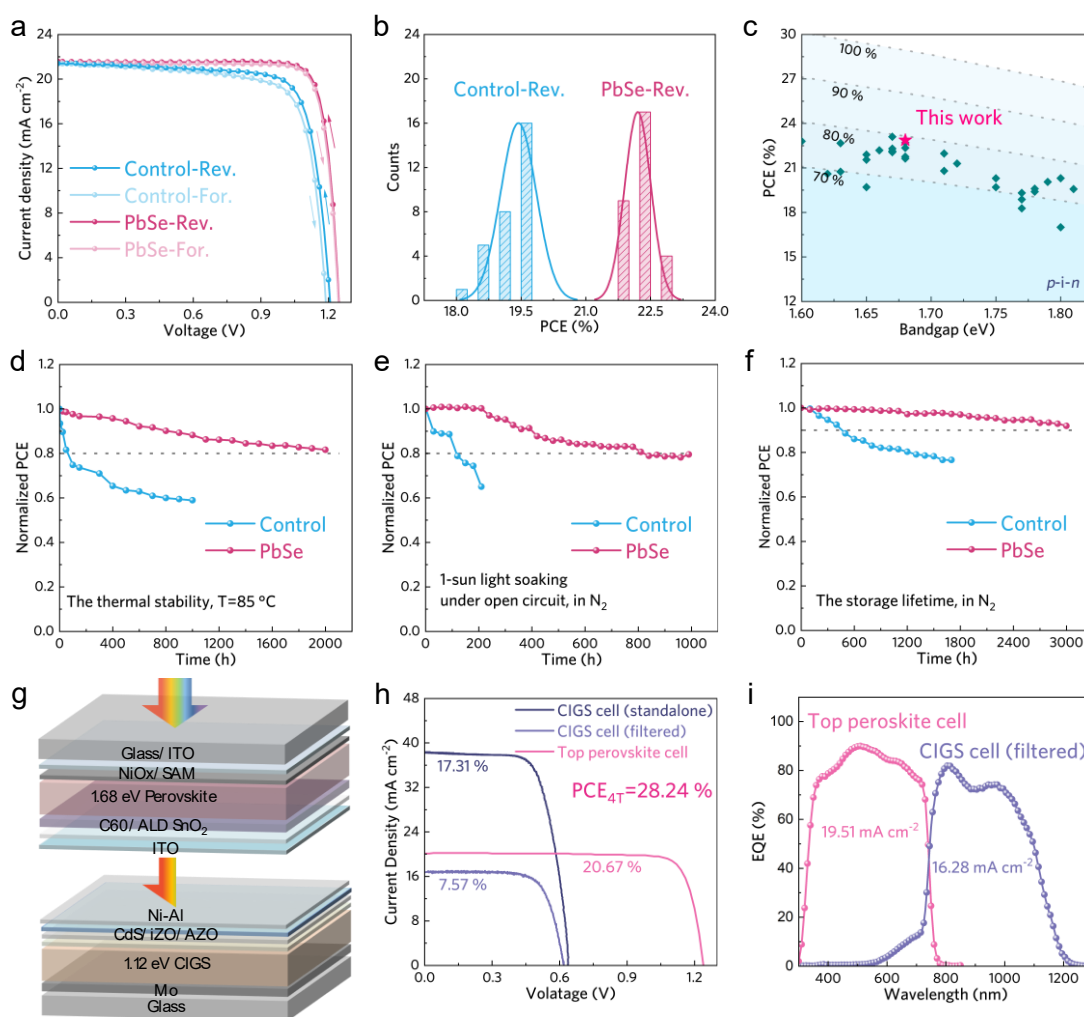


Fig. 5 The performance of solar cells. **a.** $J-V$ curves. **b.** The statistical diagram of the devices' PCEs. **c.** Summary of high-efficiency $p-i-n$ devices (PCE) reported up to date with various bandgaps (1.60-1.85 eV) compared to the thermodynamic potential limit (black lines). The detailed information is provided in **Table S6**. **d.** Thermal stability at N_2 , $T=85\text{ }^{\circ}\text{C}$. **e.** 1-sun light soaking at N_2 , $T=45\text{ }^{\circ}\text{C}$. **f.** The storage lifetimes at N_2 in dark. **g.** Schematic structure of the 4T perovskite/CIGS tandem solar cell. **h.** The $J-V$ curves of the 4T cell. **i.** EQE measurements for the tandem cell.

To apply the strategy of PbSe NCs embedment in the development of mechanically-stacked four-terminal (4T) perovskite-CIGS tandem solar cells, we proceeded to fabricate a semi-transparent cell. The 4T tandem cell consisted of a wide-bandgap (1.68 eV) perovskite top cell and a low-bandgap (1.12 eV) CIGS bottom cell, with the respective structures illustrated in **Fig. 5g**. The cross-sectional image (**Fig. S26**) delineated all the distinct layers comprising the semi-transparent cell. The wide-bandgap perovskite was discernible in the shade, affirming that the indium tin oxide (ITO) sputtering process did not compromise the integrity of the films, and vertical grains of good quality were observed within the perovskite layer⁶³. The top cell exhibited a PCE of 20.67 %, whereas the bottom cell attained a PCE of 17.31 %. Furthermore, the $J-V$ curve of the CIGS cells filtered by a semi-transparent perovskite device has been analyzed (**Fig. 5h**). As a result, the 4T tandem cell delivered an overall PCE of 28.24 %. Their corresponding photovoltaic parameters were summarized in

Table 1. The integrated J_{sc} derived from the EQE measurement (**Fig. 5i**) over the AM 1.5 G solar spectrum for the top cell and the filtered CIGS bottom cell were determined to be 19.51 mA cm^{-2} and 16.28 mA cm^{-2} , respectively.

Table 1 J - V parameters of the 4T tandem cell.

Devices	V_{oc} (V)	FF (%)	J_{sc} (mA cm^{-2})	PCE (%)
CIGS (standalone)	0.640	70.60	38.32	17.31
CGS Cell (filtered)	0.618	73.18	16.73	7.57
Semi-transparent top cell	1.24	82.94	20.10	20.67
4T tandem cell				28.24

In summary, we have successfully developed metastable PbSe NCs by LPPL and demonstrated a significant performance enhancement in the suppression of halide segregation after incorporating the PbSe NCs in the mixed-halide perovskite solar cells. We anchor halides during the crystallization process of perovskite by utilizing PbSe NCs, to fill the halide vacancies, thereby minimizing defects. The incorporation of PbSe NCs plays a crucial role in improving the photovoltaic performance of devices, and the single-junction PbSe device exhibited a record PCE of 22.87 % with a V_{oc} of 1.25 V. The device retains 79 % of its initial PCE even after undergoing 1000 h of light soaking under an open circuit, indicating superior photostability. Furthermore, the exploration extends to the realm of tandem solar cells, where we integrate PbSe NCs into 4T perovskite-CIGS tandem devices. Impressively, these devices exhibit a PCE of 28.32 %. This achievement demonstrates that introducing metastable nanocrystals can modulate the Pb-halide octahedral structure during crystallization and significantly inhibit photo-induced phase segregation. The PbSe NCs embedment and the heteroepitaxial-grown method in this study provides new insights for tandem solar cells.

Methods

Materials

The anhydrous dimethyl sulfoxide (DMSO), N, N-dimethylformamide (DMF), 2-propanol (IPA), and ethyl acetate (EA) were procured from Sigama-Aldirh. CsI, PbBr, FAI, PbI₂, MABr, phenethylammonium iodide (PEAI) and phenyl-C61-butyric acid methyl ester (PC₆₁BM), C₆₀, Bathocuproine (BCP) were brought from Xi'an Polymer Light Technology CO., Ltd. The NiO_x powder was sourced from Advanced Election Technology CO., Ltd. The MeO-2PACz was acquired from the Tokyo Chemical Industry. The PbSe powder was brought from Alfa Aesar.

Preparation of NCs in solvent

A specific quantity of powder materials is mixed with 10 mL solution of DMF: DMSO (4:1 v/v). Subsequently, it undergoes non-focusing nanosecond pulsed laser irradiation (Quantel, repetition rate: 10 Hz, pulse width: 8 ns, beam diameter: 8 mm) with a wavelength of 1064 nm. During irradiation, continuous ultrasonic treatment is applied to ensure the preparation of homogeneous and well-dispersed PbSe

colloids. Tailored laser fluence is applied, ranging from 600 mJ/pulse cm², with a consistent irradiation time of 5 minutes and a cooling temperature of 0 °C.

Fabrication of single-junction perovskite cells

The In-doped SnO₂ (ITO) glass substrates were cleaned sequentially with detergent, distilled water, isopropanol, and ethanol. After 20 minutes of UV-ozone treatment, NiO_x nanoparticles (15 mg/mL in distilled water) were spin-coated onto the ITO at 3000 rpm for 40 s and annealed at 100 °C for 5 min in ambient air. The MeO-2PACz layer (0.5 mg/mL in IPA) was deposited on the NiO_x layer at 3000 rpm for 30 s in a N₂ glove box, then annealed at 100 °C for 10 min. For the perovskite layer, a 1.5 M Cs_{0.05}(FA_{0.77}MA_{0.23})_{0.95}Pb(I_{0.77}Br_{0.23})₃ precursor solution (DMF: DMSO = 4:1, v/v) was fully stirred overnight at room temperature. It was then spin-coated at 4000 rpm for 40 s, using 200 µl of EA as the antisolvent at the 30th second. The film was annealed at 120 °C for 10 min. After coating PEAI (1 mg/mL in IPA) onto the perovskite film at 5000 rpm for 20s, the PC₆₁M (20 mg/mL in CB) layer and the BCP (0.7 mg/mL in IPA) film were spin-coated at 2000 rpm and 4000 rpm for 20s, then annealed at 70 °C for 10 min. Finally, a 100 nm thick layer of Ag was evaporated onto the active area through a mask (0.05 cm²).

Fabrication of semitransparent perovskite cells

After annealing the perovskite, a 20 nm layer of C₆₀ was thermally evaporated at a rate of 0.2 Å/s. Then a 30 nm film of SnO_x was deposited over 300 cycles using atomic layer deposition (ALD). The 100 nm ITO film was sputtering using an radio frequency (RF) power of 120 W, with a deposition time of 10 min.

Fabrication of CIGS cells

The CIGS absorption layer film was prepared using a three-stage co-evaporation process on Mo coated soda-lime glass. The conventional three-stage process is as follows: In the first step, NaF was evaporated for 7 min, followed by the evaporation of In and Ga for 36 min at a substrate temperature of approximately 370 °C. In the second step, only Cu was evaporated, and the In and Ga guards were closed (with the evaporator temperature remaining unchanged). Simultaneously, the substrate temperature was increased within 6 min to 570 °C and maintained for approximately 15 min.

After the deposition of CIGS absorber, a chemical bath deposition (CBD) method was employed to deposit a buffer layer of CdS on the surface of the CIGS absorption layer, with a thickness of approximately 50 nm.

Following this, in a vacuum chamber, an RF magnetron sputtering method was employed to deposit high-resistance i-ZnO layers with a thickness of 50 nm, as well as an AZO transparent conductive layer with a thickness of approximately 150 nm. The 100 nm Ni/10 µm Al metal grids were evaporated on top of the AZO surface by electron beam evaporation. Finally, the sample is divided into small cells with an area of 0.5 cm².

Characterization

SEM images were captured on ZEISS SUPRA. XRD images were obtained by the D8 ADVANCE. The PL and TRPL images were acquired using the FLS980. The confocal fluorescence images were obtained by the Leica TCS SP8. TEM images were performed by FEI Talos F200X TEM. XPS spectra were measured using the PHI5000

Versaprobe III, while UPS was characterized using the same instrument, PHI5000 VersaProbe III.

Device characterization

A xenon-lamp-based solar simulator (Oriel 67005, 150 W Solar Simulator) was utilized to produce simulated AM 1.5G irradiation at the intensity of 100 mW cm^{-2} for J - V measurements. The light intensity was calibrated using a silicon (Si) diode (Hamamatsu S1133) equipped with a Schott visible-color glass filter (KG5 color filter). J - V measurements were carried out with a scanning rate of 0.2 V/s using a Keithley 2420 Source Meter. External quantum efficiencies were determined using a Newport QE measurement kit by focusing a monochromatic beam of light onto the devices. For steady-state output measurements, the solar cells were exposed to simulated AM 1.5G, 1-sun illumination to record the photocurrent under a bias voltage. Periodically, the power conversion efficiencies (PCEs) of the devices were measured under AM 1.5G simulated sunlight in ambient air. The thermal stability of the non-encapsulated solar cell was evaluated on a hot plate (85°C) in a nitrogen atmosphere. Following cooling to room temperature, PCEs were periodically measured under AM 1.5G simulated sunlight.

Data availability

The data are available upon reasonable request to the corresponding authors.

References

1. Kim, D. *et al.* Efficient, stable silicon tandem cells enabled by anion-engineered wide-bandgap perovskites. *Science* **368**, 155-160 (2020).
2. Liang, H. *et al.* 29.9%-efficient, commercially viable perovskite/CuInSe₂ thin-film tandem solar cells. *Joule* **7**, 2859-2872 (2023).
3. Tang, L. *et al.* All-round passivation strategy yield flexible perovskite/CuInGaSe₂ tandem solar cells with efficiency exceeding 26.5%. *Adv. Mater.*, 10.1002/adma.202402480, (2024).
4. Li, W. *et al.* High-performance solar flow battery powered by a perovskite/silicon tandem solar cell. *Nat. Mater.* **19**, 1326-1331 (2020).
5. Duan, L. *et al.* Stability challenges for the commercialization of perovskite-silicon tandem solar cells. *Nat. Rev. Mater.* **8**, 261-281 (2023).
6. Chen, B. *et al.* Blade-coated perovskites on textured silicon for 26%-efficient monolithic perovskite/silicon tandem solar cells. *Joule* **4**, 850-864 (2020).
7. Jia, D., Chen J., Zhuang R., Hua Y., Zhang X. Antisolvent-assisted in situ cation exchange of perovskite quantum dots for efficient solar cells. *Adv. Mater.* **35**, 2212160 (2023).
8. Wang, X. *et al.* Stable cesium-rich formamidinium/cesium pure-iodide perovskites for efficient photovoltaics. *ACS Energy Lett.* **6**, 2735-2741 (2021).
9. Hoke, E. T., Slotcavage D. J., Dohner E. R., Bowring A. R., Karunadasa H. I., McGehee M. D. Reversible photo-induced trap formation in mixed-halide hybrid perovskites for photovoltaics. *Chem. Sci.* **6**, 613-617 (2015).

10. Guo, Y. *et al.* Photoinduced self-healing of halide segregation in mixed-halide perovskites. *ACS Energy Lett.* **6**, 2502-2511 (2021).
11. Aydin, E. *et al.* Interplay between temperature and bandgap energies on the outdoor performance of perovskite/silicon tandem solar cells. *Nat. Energy* **5**, 851-859 (2020).
12. De Bastiani, M. *et al.* Toward stable monolithic perovskite/silicon tandem photovoltaics: A six-month outdoor performance study in a hot and humid climate. *ACS Energy Lett.* **6**, 2944-2951 (2021).
13. Zou, Y. *et al.* A practical approach toward highly reproducible and high-quality perovskite films based on an aging treatment. *Adv. Mater.* **36**, 2307024 (2023).
14. Mao, W. *et al.* Light-induced reversal of ion segregation in mixed-halide perovskites. *Nat. Mater.* **20**, 55-61 (2020).
15. DuBose, J. T., Kamat P. V. Hole trapping in halide perovskites induces phase segregation. *Acc. Mater. Res.* **3**, 761-771 (2022).
16. Motti, S. G., Patel J. B., Oliver R. D. J., Snaith H. J., Johnston M. B., Herz L. M. Phase segregation in mixed-halide perovskites affects charge-carrier dynamics while preserving mobility. *Nat. Commun.* **12**, 6955 (2021).
17. Xu, W. *et al.* Suppressing defects-induced nonradiative recombination for efficient perovskite solar cells through green antisolvent engineering. *Adv. Mater.* **32**, 2003965 (2020).
18. Tavakoli, M. M. *et al.* Controllable perovskite crystallization via antisolvent technique using chloride additives for highly efficient planar perovskite solar cells. *Adv. Energy Mater.* **9**, 1803587 (2019).
19. Cho, J., Kamat P. V. How chloride suppresses photoinduced phase segregation in mixed halide perovskites. *Chem. Mater.* **32**, 6206-6212 (2020).
20. Azhar, M. *et al.* Damping the phase segregation in mixed halide perovskites: Influence of x-site anion. *Mater. Chem. Phys.* **287**, 126335 (2022).
21. Yi, C. *et al.* Entropic stabilization of mixed a-cation ABX₃ metal halide perovskites for high performance perovskite solar cells. *Energy Environ. Sci.* **9**, 656-662 (2016).
22. Meloni, S. *et al.* Ionic polarization-induced current-voltage hysteresis in CH₃NH₃PbX₃ perovskite solar cells. *Nat. Commun.* **7**, 10334 (2016).
23. Barker, A. J. *et al.* Defect-assisted photoinduced halide segregation in mixed-halide perovskite thin films. *ACS Energy Lett.* **2**, 1416-1424 (2017).
24. Bai, Y. *et al.* Initializing film homogeneity to retard phase segregation for stable perovskite solar cells. *Science* **378**, 747-754 (2022).
25. Draguta, S. *et al.* Rationalizing the light-induced phase separation of mixed halide organic–inorganic perovskites. *Nat. Commun.* **8**, 200 (2017).
26. Bai, Y. *et al.* A pure and stable intermediate phase is key to growing aligned and vertically monolithic perovskite crystals for efficient PIN planar perovskite solar cells with high processibility and stability. *Nano Energy* **34**, 58-68 (2017).
27. Ji, S. G. *et al.* Stable pure-iodide wide-band-gap perovskites for efficient Si tandem cells via kinetically controlled phase evolution. *Joule* **6**, 2390-2405 (2022).
28. Tao, J. *et al.* F-type pseudo-halide anions for high-efficiency and stable wide-band-

- gap inverted perovskite solar cells with fill factor exceeding 84%. *ACS Nano* **16**, 10798-10810 (2022).
29. Yang, G. *et al.* Defect engineering in wide-bandgap perovskites for efficient perovskite–silicon tandem solar cells. *Nat. Photonics* **16**, 588-594 (2022).
 30. Meng, X. *et al.* Effective inhibition of phase segregation in wide-bandgap perovskites with alkali halides additives to improve the stability of solar cells. *Sol. RRL* **7**, 2201099 (2023).
 31. Abdi-Jalebi, M. *et al.* Maximizing and stabilizing luminescence from halide perovskites with potassium passivation. *Nature* **555**, 497-501 (2018).
 32. Wang, L. *et al.* Strain modulation for light-stable n-i-p perovskite/silicon tandem solar cells. *Adv. Mater.* **34**, 2201315 (2022).
 33. Ning, Z. *et al.* Quantum-dot-in-perovskite solids. *Nature* **523**, 324-328 (2015).
 34. Guo, P. *et al.* Laser manufactured nano-Mxenes with tailored halogen terminations enable interfacial ionic stabilization of high performance perovskite solar cells. *Adv. Energy Mater.* **12**, 2202395 (2022).
 35. Guo, P. *et al.* Interfacial embedding of laser-manufactured fluorinated gold clusters enabling stable perovskite solar cells with efficiency over 24%. *Adv. Mater.* **33**, 2101590 (2021).
 36. Zhao, W. *et al.* Laser derived electron transport layers with embedded p-n heterointerfaces enabling planar perovskite solar cells with efficiency over 25%. *Adv. Mater.* **35**, 2300403 (2023).
 37. Jian, J. *et al.* Embedding laser generated nanocrystals in Bivo(4) photoanode for efficient photoelectrochemical water splitting. *Nat. Commun.* **10**, 2609 (2019).
 38. Yang, W. *et al.* Unlocking voltage potentials of mixed-halide perovskite solar cells via phase segregation suppression. *Adv. Funct. Mater.* **32**, 2110698 (2021).
 39. Guo, P. *et al.* Laser-generated nanocrystals in perovskite: Universal embedding of ligand-free and sub-10 nm nanocrystals in solution-processed metal halide perovskite films for effectively modulated optoelectronic performance. *Adv. Energy Mater.* **9**, 1901341 (2019).
 40. Yang, X. *et al.* Grain-boundaries-engineering via laser manufactured La-doped BaSnO₃ nanocrystals with tailored surface states enabling perovskite solar cells with efficiency of 23.74%. *Adv. Funct. Mater.* **32**, 2112388 (2022).
 41. Yu, H. *et al.* Laser-generated supranano liquid metal as efficient electron mediator in hybrid perovskite solar cells. *Adv. Mater.* **32**, 2001571 (2020).
 42. Sarkar, S. K. *et al.* Effects of solution pH and surface chemistry on the postdeposition growth of chemical bath deposited PbSe nanocrystalline films. *Chem. Mater.* **19**, 879-888 (2007).
 43. Canava, B., Vigneron J., Etcheberry A., Guillemoles J. F., Lincot D. High resolution Xps studies of Se chemistry of a Cu(In, Ga)Se₂ surface. *Appl. Surf. Sci.* **202**, 8-14 (2002).
 44. Wu, W., Tang Y., Li B., Xiang X., Liu C., Zu X. Microstructure and optical properties of pbse nanocrystalline films prepared by magnetron sputtering. *Opt. Mater.* **118**, 111233 (2021).
 45. Xie, Y., Su H., Li B., Qian Y. A direct solvothermal route to nanocrystalline

- selenides at low temperature. *Mater. Res. Bull.* **35**, 459-464 (2000).
46. Mohammadi-Jam, S., Waters K. E., Greenwood R. W. A review of zeta potential measurements using electroacoustics. *Adv. Colloid Interface Sci.* **309**, 102778 (2022).
 47. Wei, B. *et al.* Effect of pHs on dispersity of maize starch nanocrystals in aqueous medium. *Food Hydrocoll.* **36**, 369-373 (2014).
 48. Belisle, R. A., Bush K. A., Bertoluzzi L., Gold-Parker A., Toney M. F., McGehee M. D. Impact of surfaces on photoinduced halide segregation in mixed-halide perovskites. *ACS Energy Lett.* **3**, 2694-2700 (2018).
 49. Brennan, M. C., Draguta S., Kamat P. V., Kuno M. Light-induced anion phase segregation in mixed halide perovskites. *ACS Energy Lett.* **3**, 204-213 (2017).
 50. Bush, K. A. *et al.* Compositional engineering for efficient wide band gap perovskites with improved stability to photoinduced phase segregation. *ACS Energy Lett.* **3**, 428-435 (2018).
 51. Kang, D.-H., Lee S.-U., Park N.-G. Effect of residual chloride in FAPbI₃ film on photovoltaic performance and stability of perovskite solar cell. *ACS Energy Lett.* **8**, 2122-2129 (2023).
 52. Kim, G., Min H., Lee K. S., Lee D. Y., Yoon S. M., Seok S. I. Impact of strain relaxation on performance of α -formamidinium lead iodide perovskite solar cells. **370**, 108-112 (2020).
 53. Bischak, C. G. *et al.* Origin of reversible photoinduced phase separation in hybrid perovskites. *Nano Lett.* **17**, 1028-1033 (2017).
 54. Ma, Q. *et al.* One-step dual-additive passivated wide-bandgap perovskites to realize 44.72%-efficient indoor photovoltaics. *Energy Environ. Sci.* **17**, 1637-1644 (2024).
 55. Song, Z. *et al.* Inverted wide-bandgap 2D/3D perovskite solar cells with >22% efficiency and low voltage loss. *Nano Lett.* **23**, 6705-6712 (2023).
 56. Su, G. *et al.* Crystallization regulation and defect passivation for efficient inverted wide-bandgap perovskite solar cells with over 21% efficiency. *Adv. Energy Mater.* **14**, (2023).
 57. Yi, Z. *et al.* Achieving a high open-circuit voltage of 1.339 V in 1.77 eV wide-bandgap perovskite solar cells via self-assembled monolayers. *Energy Environ. Sci.* **17**, 202-209 (2024).
 58. Yang, L. *et al.* Suppressing halide segregation via pyridine-derivative isomers enables efficient 1.68 eV bandgap perovskite solar cells. *Advanced Materials*, 10.1002/adma.202311923, (2024).
 59. Li, M. H. *et al.* Electrical loss management by molecularly manipulating dopant-free poly(3-hexylthiophene) towards 16.93 % CsPbI₂Br solar cells. *Angew. Chem. Int. Ed.* **60**, 16388-16393 (2021).
 60. Ye, L. *et al.* Managing secondary phase lead iodide in hybrid perovskites via surface reconstruction for high-performance perovskite solar cells with robust environmental stability. *Angew. Chem. Int. Ed.* **62**, e202300678 (2023).
 61. Bu, T. *et al.* Universal passivation strategy to slot-die printed SnO₂ for hysteresis-free efficient flexible perovskite solar module. *Nat. Commun.* **9**, 4609 (2018).
 62. Yan, N. *et al.* Wide-bandgap perovskite solar cell using a fluoride-assisted surface

- gradient passivation strategy. *Angew. Chem. Int. Ed.* **62**, e202216668 (2023).
63. Singha, A. *et al.* Stable and efficient large-area 4T Si/perovskite tandem photovoltaics with sputtered transparent contact. *Solar RRL* **7**, 230017 (2023).

Acknowledgements

The authors acknowledge fruitful discussions with Assoc. Prof. Qian Ye from NPU, Dr. Xiaoning Zhu and Dr. Linqun Huang from New Energy Institute in Shaanxi Coal and Chemical Technology Research Institute.

Funding: National Natural Science Foundation of China (NSFC) grant (Award No. 52202115 (P.G.), 52103286 (Z. Liu), and 52172101 (H.W.)); Shaanxi Bureau of Science and Technology (Award No. 2022KWZ-07).

“Shccig-Qinling Program” under the contract No. SMYJY202300321C.

Author contributions

H.W. and Z. Liu conceived the idea and designed the experiments. Y.J. conducted the experiments under the supervision of P.G., H.W. and Z. Liu. Y.J. wrote the first draft and Z. Liu wrote the final manuscript. Y.J. and L.D. conducted the semi-transparent cells (under the supervision of Z. Liu and Z. Li). X.S. conducted the CIGS cells under the supervision of W.L. X.H.Z., Y.Z., N.J., Z.F., L.M., X.Z. and R.C. assisted in preparing samples and performing the characterization. P.G., Y.H., F.L. and H.W. helped to modify the manuscript. All authors contributed to analyzing and discussing the results.

Competing interests

The authors declare no competing interests.

Additional information

Supplementary information The online version contains supplementary material available at: